Applied Energy 240 (2019) 399–408

Contents lists available at ScienceDirect

Applied Energy

journal homepage: www.elsevier.com/locate/apenergy

Leidenfrost heat engine: Sustained rotation of levitating rotors on turbine-inspired substrates

Prashant Agrawal[a,*], Gary G. Wells[a], Rodrigo Ledesma-Aguilar[a], Glen McHale[a], Anthony Buchoux[b], Adam Stokes[c], Khellil Sefiane[b]

[a] Smart Materials & Surfaces Laboratory, Faculty of Engineering & Environment, Northumbria University, Newcastle upon Tyne NE1 8ST, UK
[b] School of Engineering, Institute for Multiscale Thermofluids, The University of Edinburgh, The King's Buildings, Edinburgh EH9 3LJ, UK
[c] School of Engineering, Institute for Integrated Micro and Nano Systems, The University of Edinburgh, The King's Buildings, Edinburgh EH9 3LJ, UK

HIGHLIGHTS

- We show the continuous operation of a conceptual heat engine using Leidenfrost effect.
- Thin-film boiling is used to rotate a liquid supporting a solid on turbine-like substrates.
- The rotation stability increases by increasing the wettability of the solid.
- We use superhydrophobic coatings to show rotation below the Leidenfrost temperature.
- An analytical model is used to characterize rotation over a wide temperature range.

ARTICLE INFO

Keywords:
Leidenfrost
Wettability
Droplet
Heat transfer
Heat engine
Thin-film boiling
Vapor bearing

ABSTRACT

The prospect of thermal energy harvesting in extreme environments, such as in space or at microscales, offers unique opportunities and challenges for the development of alternate energy conversion technologies. At microscales mechanical friction presents a challenge in the form of energy losses and wear, while presence of high temperature differences and locally available resources inspire the development of new types of heat engines for space and planetary exploration. Recently, levitation using thin-film boiling, *via* the Leidenfrost effect, has been explored to convert thermal energy to mechanical motion, establishing the basis for novel reduced-friction heat engines. In the Leidenfrost effect, instantaneous thin-film boiling occurs between a droplet and a heated surface, thereby levitating the droplet on its own vapor. This droplet state provides virtually frictionless motion and self-propulsion, whose direction can be designed into the system by asymmetrically texturing the substrate. However, sustaining such thermal to mechanical energy conversion is challenging because the Leidenfrost transition temperature for water on a smooth metal surface is ~220 °C and, despite the low thermal conductivity of the vapor layer, the droplet continuously evaporates. Further challenges include effective transfer of thermal energy into rotational, rather than linear motion, and driving solid components and not simply droplets.

Here we present a Leidenfrost rotor, where a solid component is coupled to a rotating liquid volume using surface tension and levitated in continuous operation over a turbine-inspired substrate. We address two key challenges: we show how the liquid can be replenished to achieve the continuous operation of the device; and we show how a superhydrophobic coating to the substrate can broaden the temperature range of operation and the stability of the rotor. Because the liquid acts as a working substance by extracting heat from the substrate to produce useful work in the form of rotation of the coupled solid component, our results demonstrate that a Leidenfrost engine operating in a closed thermodynamic cycle is possible.

1. Introduction

Heat engines are versatile thermal energy conversion systems with a wide range of applicability from gas based internal combustion engines to phase change dependent steam engines. The ability to use different working substances makes them versatile for energy conversion in different environments and applications. For instance, steam powered engines have exploited the abundance of water as a favourable working

* Corresponding author.
E-mail address: prashant.agrawal@northumbria.ac.uk (P. Agrawal).

https://doi.org/10.1016/j.apenergy.2019.02.034
Received 19 November 2018; Received in revised form 2 February 2019; Accepted 6 February 2019

fluid for large scale power generation, while hydrocarbons can be used for low grade waste energy recovery [1,2]. Hence, potential future applications in space and planetary exploration will rely on locally available resources as a means of reducing material transportation costs [3,4]. In addition, presence of extreme temperature differences and pressures can support the use of heat engines for power generation in such environments. Another extreme environment where the potential of heat engines as thermal energy harvesters can be explored is in microscale systems. Here, due to a high surface area to volume ratio, friction causes significant wear and energy losses [5,6], which restricts the sustained conversion of thermal to mechanical energy.

Recently, thin-film boiling, via the Leidenfrost effect [7], has been demonstrated as a promising concept for converting thermal energy to mechanical motion [8]. In this approach, when a liquid droplet touches a surface heated to a temperature significantly higher than the liquid's boiling point, a vapor layer is produced instantly between the droplet and the heated surface (at typically 220 °C for water). The same effect can also be observed for alternate liquids [9,10] and solids, e.g. dry-ice, undergoing sublimation [11,12]. In both cases, the vapor layer acts as a thermal insulator that reduces the evaporation rate of the self-levitating liquid or solid, as well as a bearing that virtually eliminates friction. On a smooth flat surface, the exiting vapor is expelled out symmetrically from the base of the levitating liquid or solid volume [13]. By introducing an asymmetry in the vapor flow, low-friction self-propulsion of liquid droplets [8,14] and solid blocks [15] can be achieved. The combination of low-friction and the ease of employing alternate working liquids (or solids) provides opportunities for new approaches for heat to motion conversion in extreme environments. In addition to their low-friction characteristics, which may have advantages in micro-engines, Leidenfrost self-propulsion has potential applications in deep space and planetary exploration [16]. Heat engines based on Leidenfrost self-propulsion can utilize heat cycles of naturally occurring alternative working substances [3,12,16], such as ices of H_2O, CO_2 and CH_4, in extreme conditions of low pressure and high temperature differences for thermal energy harvesting. The low gravity environment can further assist in reducing the energy cost of levitation.

Several underlying mechanisms have been proposed for Leidenfrost self-propulsion, including Marangoni flows [17], jet thrust [11], drag force due to thermal creep induced flows [18] and drag force due to vapor rectification [8,19]. Of these, self-propulsion based on viscous friction is the most widely studied and has been used to explain the motion of both levitating liquids and solids. Numerical [20,21] and analytical models [15,19,22] have been corroborated with experimental observations [19,20,22]. In this case, the asymmetry in the substrate rectifies the exiting vapor flow in a specific direction producing a viscous drag force on the levitating liquid or solid propelling it in the direction of the vapor flow [8,11,20]. Using this principle, self-propulsion of evaporating liquids [8] and sublimating solids [20] has been demonstrated on substrates textured as ratchets [15,21,23,24], herringbones [19] and on asymmetric nanostructured substrates [25]. Self-propulsion can also be obtained by introducing an asymmetry in the levitating component. For example, cylindrical blocks of dry-ice self-propel on a smooth flat surface when an asymmetry in their mass distribution is introduced [26]. The asymmetric mass tilts the base of the levitating component, where the resulting asymmetric vapor flow leads to self-propulsion. Similar asymmetric vapor flows have been recently shown to self-propel small droplets (typically millimetre size) on smooth surfaces [14]. Large, gravity flattened drops have symmetric counter-rotating internal flows. As the droplet size decreases, this flow symmetry breaks resulting in a single rotating cell, like a wheel. This rolling liquid-vapor interface entrains air which tilts the droplet's base leading to an asymmetric expulsion of vapor, which propels the droplet [14].

Beyond linear translational motion, but to a much lesser extent, the concept of Leidenfrost levitation and self-propulsion has been used to demonstrate the rotation of liquids and solids. Studies have reported the rotation of dry ice and droplets on turbine-like substrates [22] to produce a net torque, rotation of dry-ice platelets linked by an off centered rod [26] and windmill textures [27] to rotate air-levitated non-volatile solids. Previous studies demonstrate that the Leidenfrost effect can be used to convert thermal energy to mechanical and electrical energy. Additionally, the propulsion force can be transferred to translate [26,28,29] or rotate [22] non-volatile objects. The transfer of torque from the working substance (phase changing solid or liquid) to additional solid components provides the basis of developing a mechanical and heat engine using the Leidenfrost effect [22].

However, a key challenge yet to be achieved is the continuous operation of a Leidenfrost engine within a closed thermodynamic cycle, where the working substance can be replenished continuously. An effective coupling between the working substance and the solid components also becomes critical for energy transfer, especially in the case of a liquid working substance. Lowering the operating temperature [30] or heat input [31] is also desirable [32,33]. The Leidenfrost temperature can be altered by changing the ambient pressure [34–37] or by modifying the surface wettability [38–42]. To reduce the operating temperature, the ambient pressure can be reduced [34] or a superhydrophobic coating applied to a substrate [30]. This latter approach smooths the Leidenfrost transition as a function of temperature [38] and enables droplet propulsion at temperatures lower than the boiling point of the liquid [30].

In this work, we demonstrate the sustained rotation of a Leidenfrost rotor: a coupled liquid-solid system held together by surface tension forces, on a heated turbine-inspired substrate. The rotation of the levitating rotor is sustained at a constant angular speed by continuously replenishing the evaporating liquid, which provides the working substance for a closed thermodynamic cycle. Due to the high vapor pressure from the thin-film boiling near the substrate, the coupling liquid is susceptible to vapor bubble formation [43–45]. This bubble formation affects the stability of the liquid volume and, hence, the steady-state torque and angular speed of the coupled solid rotor component. We show that the vapor bubble formation can be reduced by enhancing the solid-liquid coupling. The solid component is made more hydrophilic or superhydrophilic to improve liquid adhesion *via* improved wettability, resulting in a stabile rotation of the Leidenfrost rotor. We also control the vapor bubble formation by reducing the vapor pressure, which we achieve by lowering the operating temperature and by changing the substrate geometry. Finally, we provide a model for characterizing the steady-state angular velocity and torque and analyze the rotation of the rotor across a wide temperature range to identify the optimum operating conditions for the Leidenfrost rotors.

2. Thermodynamic cycle concept

Our thermodynamic cycle for a Leidenfrost rotor is similar to a Rankine cycle which operates on the phase change of a liquid working substance [22]. The thermodynamic transformations that a working substance goes through in a closed Rankine cycle are shown in Fig. 1(a). In such a cycle, the liquid working substance is pressurized and fed to a boiler, where it absorbs heat from a heat source (e.g. through fuel combustion, geothermal energy or solar energy) and undergoes a phase change into vapor. This vapor is passed through a turbine to produce work. The working substance undergoes a phase change back to the liquid state in the condenser by releasing heat to a heat sink (environment or heat exchanger) and is fed back to the pump for recirculation. A major difference in the thermodynamic cycle of a Leidenfrost rotor compared to this traditional Rankine cycle is that the heat input (phase change) and work output operations on the working substance are performed in a single stage (Fig. 1(b)), i.e. over the heated substrate. This arrangement has the benefits of a smaller footprint and, therefore, of reduced losses from transportation of the working substance between units. In our experimental realization of this Leidenfrost rotor (Fig. 1(c)) the liquid working substance is deposited on

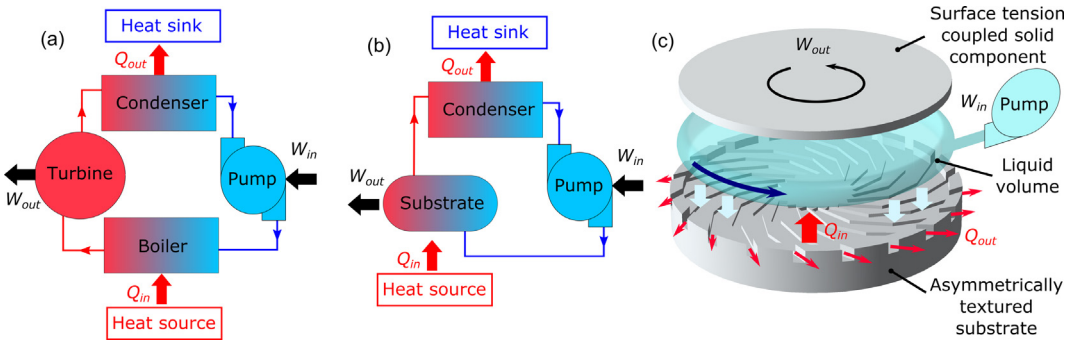

Fig. 1. (a) Depiction of the circulation of a working substance in a Rankine cycle. The working liquid is heated from a heat source and undergoes a phase change in the boiler, the resulting vapor expands to produce work in the turbine, loses its heat to a heat sink, is compressed to change phase into a liquid, and is re-circulated to the boiler. (b) Concept of a continuously operating Leidenfrost rotor. The phase change and work production take place simultaneously in a single stage on the substrate. (c) Experimental realization of a continuously operating Leidenfrost rotor. The liquid working substance is supplied through a pump and undergoes a phase change over the substrate. The substrate also rectifies the vapor to produce work, which is observed as the rotation of the solid component coupled to the liquid volume via surface tension.

the heated turbine-inspired substrate through a pump. The substrate simultaneously vaporises the liquid and extracts work by rectifying the vapor flow. On exiting the substrate radially, the vapor could be condensed by losing heat to the surroundings and fed back into the system for recirculation, thereby completing the cycle. The maximum theoretical efficiency of this Leidenfrost rotor cycle is equal to that of a Carnot cycle working between a heat source (at temperature T_{so}) and a heat sink (at temperature T_{si}), given by: $\eta = 1 - T_{si}/T_{so}$. At the Leidenfrost temperature of water on stainless steel, around 250 °C, and ambient temperature of around 25 °C, the theoretical maximum efficiency of this cycle is about 40%. Operating beyond the Leidenfrost point will increase the ideal theoretical efficiency of the cycle. However, the practical efficiency of the cycle will depend on additional energy losses due to the dynamics of the Leidenfrost rotor.

3. Experimental method

Our Leidenfrost rotor consists of a volume of water levitating over a heated turbine-inspired substrate and supporting a thin circular solid glass plate (thickness h_p= 1 mm and radius R= 15 mm), as shown in Fig. 1(c). The aluminium turbine-inspired substrates were machined using Computer Numerical Controlled (CNC) machining to produce grooves of rectangular cross-section (width W=1 mm and depth of either D= 100 µm or 500 µm). The groove arc consists of three straight lines of length 5 mm at an angle α=45° to the radial direction, as depicted in Fig. 2(a). The substrate on which the liquid volume levitates has a radius R=15 mm. The radially outward vapor flow due to evaporation and centrifugal force from the rotation destabilize the rotation

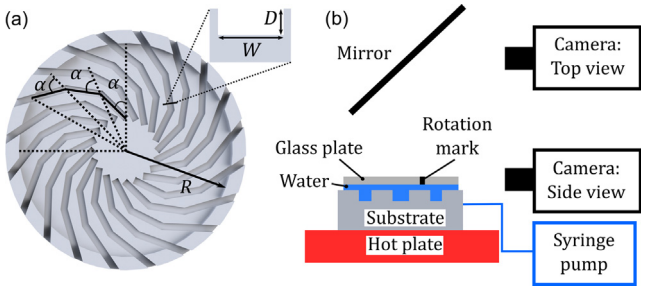

Fig. 2. (a) Depiction of turbine-inspired geometry with a rectangular cross-section groove with depth D and width W. The groove arc consists of 3 straight lines of length 5 mm. The lines make an angle $\alpha = 45°$ with the radial coordinate as shown. (b) Depiction of the experimental setup. The rotation of the glass plate, supported on the levitating liquid volume, was observed from the top and the side to ascertain the rotation speed and the variation of the water volume over time.

about the substrate axis. Therefore, the substrate has an additional raised ring at the circumference (of width 2 mm and a raised height of 1 mm) which confines the liquid volume and keeps the rotating components centred [22]. Additional grooves were machined on the raised section of the ring to insert a needle, which continuously feeds water from a syringe pump (Cole Parmer single-syringe infusion pump). Such an arrangement ensures the needle does not interfere with the rotating glass plate. The glass plates were cleaned using two different methods: (1) rinsing with isopropyl alcohol (IPA) and de-ionized (DI) water and then dried using compressed air; (2) plasma-cleaning for 30 s at 100% power (Henniker Plasma HPT-100). The latter method was used to make the glass plate superhydrophilic and, therefore, to enhance its coupling with the liquid. We also tested roughening the lower surface of the glass plate prior to plasma-cleaning to enhance coupling further through a super-hydrophilic effect and this improved the stability of rotation. However, it also led to cracks developing during Leidenfrost operation.

To operate below the usual Leidenfrost transition temperature, the turbine-inspired substrates were made superhydrophobic by spray coating a nanoparticle-based treatment (Glaco™ Mirror Coat “Zero” from Soft99 Co), using a process similar to that used by Dupeux et al. [30]. The solution was sprayed on the substrate, which was then dried for half an hour at 150 °C. The process was repeated 4 times to provide a uniform coating. To characterize the wettability of the samples produced from this coating process, the coating was applied on a flat polished aluminium substrate. Using a drop shape analyser (Kruss DSA 30), we measured an advancing contact angle of 165 ± 1° and a receding contact angle of 162 ± 1°, implying a reduced adhesion with water. The superhydrophobic coating breaks after repeated cycles of heating, especially above 200 °C. Below the Leidenfrost temperature, the disintegration of the coating leads to contact boiling of water on the substrate, which can be identified from ejection of droplets, noise and a rapid decrease in the liquid volume underneath the plate over time. Experiments performed above the Leidenfrost temperature did not show any signs of contact boiling, which suggest a marginal effect of the coating on the levitation properties in the Leidenfrost regime. To ensure reliability in the obtained results, each coated sample was subjected to a maximum of 3 heating cycles, ensuring that contact boiling did not influence the results. For experiments above the Leidenfrost temperature, freshly coated samples were used for each experiment.

The substrate was heated using a hotplate (Stuart UC 150) and its temperature monitored by placing a K-type thermocouple at its side. The substrate was kept on an aluminium block (of diameter 65 mm and thickness 10 mm) on the hot plate, which acts as a stabilizing thermal mass reducing temperature fluctuations from the hot plate. After the substrate was heated to a desired temperature, a fixed volume of water

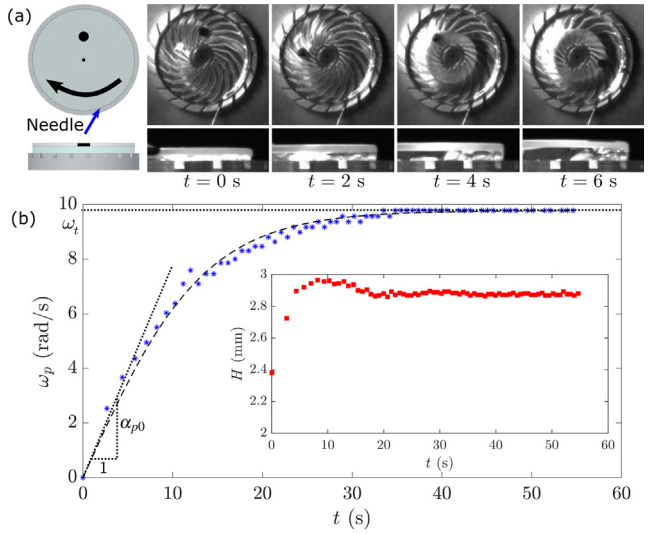

Fig. 3. Time-lapse of rotation of a glass plate supported on a water volume which is levitating over the heated turbine-inspired textured substrate with radius R=15 mm, groove depth D=100 μm at temperature T = 245°C (Supplementary video 1): (a) Experimental images of the top and side view. (b) Time evolution of the angular speed of the plate (ω_p), showing a tanh fit (dashed line) to the experimental data (blue points). The slope at t=0 gives the acceleration of the plate α_{p0} and the constant angular speed at longer times is the terminal angular speed of rotation ω_t. The inset shows the time evolution of the height of the water volume (H) obtained from the side view, which attains a constant value after the rotation stabilizes.

(1–2 ml) was deposited on the substrate. The addition of water suddenly reduces the observed temperature by about 10–30 °C, depending on the initial temperature of the substrate. The glass plate was then placed on the water volume, ensuring there was no spillage onto the top of the glass plate. The temperature was monitored for the entire experiment and varied within ± 5 °C. The flow rate was calibrated for each operating temperature to ensure the volume of water remained stable over time. The rotation of the glass plate was recorded simultaneously from the top and the side using two cameras (IDS imaging systems), to monitor the speed of rotation and liquid volume, as shown in Fig. 2(b). The videos were recorded at 70 frames per second and the rotation speed was determined from the time between two instances of visualising a black mark on the plate in the side view.

4. Experimental results

Fig. 3(a) shows an example top and side view of rotation of the glass plate cleaned by IPA and DI-water. From the initiation of motion to steady-state operation, the water lost as vapor is continuously replenished by the syringe pump. The rotation of the plate is identified by a black mark on the top and side of the plate. The speed of the plate increases with time before attaining a constant angular speed, referred to as the terminal angular speed (Fig. 3(b)).

4.1. Sustained rotation of a Leidenfrost rotor

The torque from the escaping vapor accelerates the coupled liquid-solid component, while dissipative forces in the form of inertial friction (proportional to the square of the speed [11,19]) limit its rotation speed. Considering the inertia of the coupled liquid-solid components (I), the general equation of rotation of the rotor components can be written as:

$$I\dot{\omega} = \Gamma_v - c_i\omega^2, \tag{1}$$

where, Γ_v is the driving torque from the vapor flow, ω is the average angular speed of the levitating component and c_i is the inertial resistance during rotation. The solution to the above equation for the angular speed is:

$$\omega = \omega_t \tanh(t/\tau), \begin{cases} \text{as } t \to 0;\ \omega \to \omega_t t/\tau \\ \text{as } t \to \infty;\ \omega \to \omega_t \end{cases} \tag{2}$$

where, $\omega_t = \sqrt{\Gamma_v/c_i}$ and $\tau = I/\sqrt{\Gamma_v c_i}$. According to Eq. (2) the angular speed of the plate increases with time and then attains a constant terminal angular speed ω_t. We fit our experimental data with Eq. (2) to determine the terminal speed of the plate and the torque on the plate from the rotation. The fit agrees well with the experimental data as shown in Fig. 3(b) and provides measurements of ω_t and τ. From these measurements, the torque on the plate at time t = 0 can then be obtained as $\Gamma_{p0} = I_p\alpha_{p0} = I_p\omega_t/\tau$.

The supply of liquid from the syringe pump was adjusted to balance the water lost as vapor and ensure a constant volume of the liquid, which is the working substance. The flow rate for a constant volume depends on the operating temperature and was found by repeated experiments at different temperatures (Fig. S1 in Supplementary information). The liquid-vapor interface underneath a Leidenfrost drop deforms because of the high pressure of the escaping vapor [46,47]. When this vapor pressure overcomes the hydrostatic pressure from the droplet, bubbles are created in the liquid-volume [13,48]. Similarly, Fig. 3(a) shows how, as the plate accelerates, a vapor bubble develops at the centre. As the bubble size increases, it contacts the plate, which breaks the liquid film. Subsequently, the liquid de-wets and forms a torus (Fig. 3(a)). The formation of the bubble redistributes the liquid over the substrate which is seen as a transient increase in the height of the plate (inset of Fig. 3(b)). Once the size of the bubble stabilizes, the plate height remains constant over time, which indicates a constant liquid volume. By continuously replenishing the liquid and maintaining a constant volume, the rotation can be sustained at a constant speed indefinitely.

4.2. Enhanced solid-liquid coupling

The formation of the vapor bubble and the subsequent liquid redistribution (seen in Fig. 4(a)) leads to an unstable plate rotation, as seen in Supplementary video 2. The radial displacement amplitude of the glass plate was approximately 0.4 ± 0.1 mm and the vertical displacement amplitude of the edge of the glass plate was 0.2 ± 0.1 mm, when rotating at terminal angular speed. To maintain a complete liquid film coverage on the plate, we cleaned the glass plate using a plasma treatment to increase its wettability. Supplementary video 3 shows the rotation of the plasma cleaned glass plate. Although a vapor bubble is still faintly visible under the plasma treated glass plate in Fig. 4(b), the plate rotation (seen in Supplementary video 3) is relatively more stable compared to the untreated glass plate under the same operating conditions. With plasma cleaning, the plate rotation demonstrated no measurable radial or vertical displacement at terminal angular speed. The terminal speed and torque also show a slight increase relative to the IPA and DI water rinsed glass plates (Fig. 5).

Another method to maintain a solid-liquid coupling is to suppress the formation of the vapor bubble by reducing the pressure at the centre of the substrate. This can be achieved by lowering the substrate temperature. To obtain propulsion at temperatures below the Leidenfrost temperature, the substrates were made superhydrophobic as discussed in Section 3. Fig. 4(c) shows rotation of the plate on a substrate with D = 100 μm for a temperature range of 130–340 °C. Although the vapor bubble forms at substrate temperatures as low as 130 °C, its size decreases with decreasing temperature, which is indicative of the decreasing pressure. To further decrease the pressure, the groove depth was altered. An increase in the groove depth increases the vapor layer thickness which lowers the average vapor pressure at the centre of the substrate [11,13,22]. As seen in Fig. 4(d), in the case of a substrate with groove depth D= 500 μm, the vapor bubble does not form for substrate

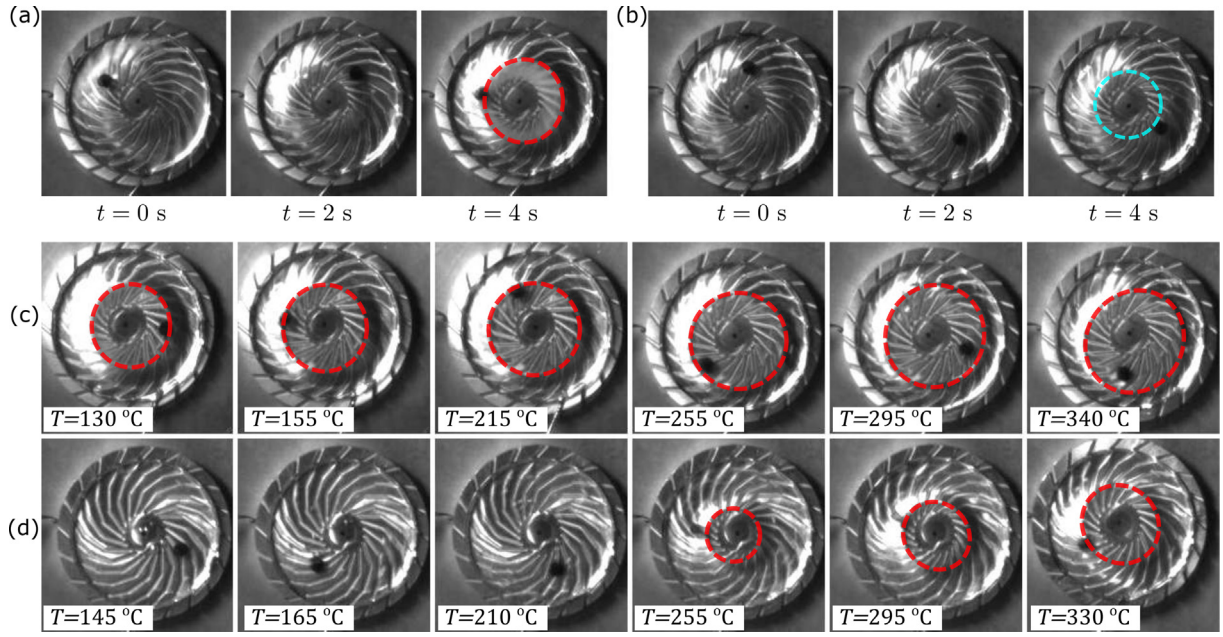

Fig. 4. Suppressing the vapor bubble formation by changing the wettability of the glass plate: (a) Rotation of IPA and DI water rinsed glass plates at T = 300°C on a substrate with D = 100 μm (b) Rotation of plasma cleaned glass plates (superhydrophilic) at T = 300°C on a substrate with D = 100 μm. Suppressing the vapor bubble formation by changing the groove depth and substrate temperature: (c) Top-view of the plate on a superhydrophobic coated substrate with D = 100 μm at different temperatures, (d) Top-view of the plate on a superhydrophobic coated substrate with D = 500 μm at different temperatures. Images are taken after 25 s of experiment run-time. The dashed red line indicates the shape of the vapor bubble. The faint vapour bubble underneath the plasma etched glass plate is indicated in a dashed blue line in (b).

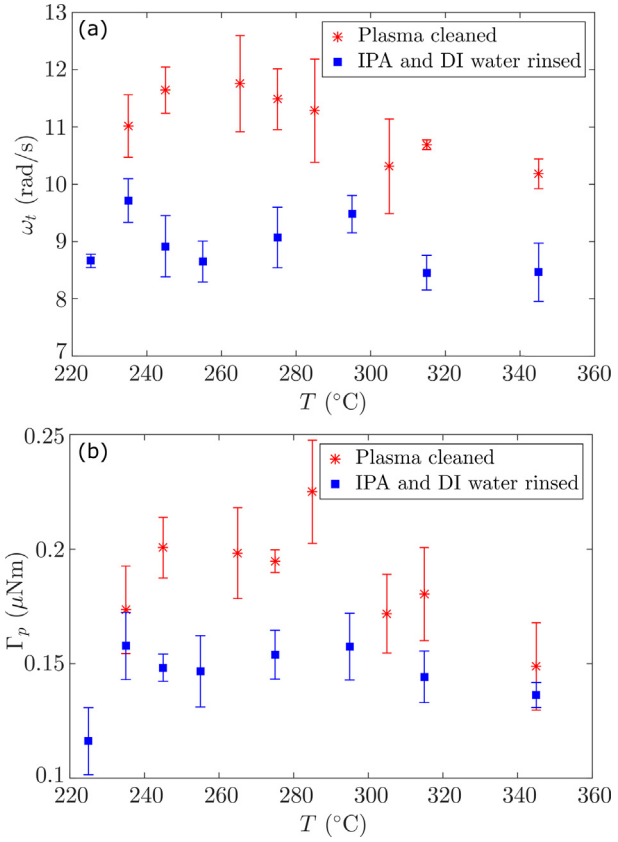

Fig. 5. Variation of (a) terminal angular speed ω_t, (b) torque Γ_{p0} with temperature for plasma cleaned glass plate compared to a glass plate rinsed with Isopropyl alcohol (IPA) and de-ionized (DI) water. The variation in temperature is ± 5 °C.

temperatures below 255 °C. Above this temperature, a vapor bubble forms and grows with increasing temperature. Although the vapor bubble formation is reduced at lower temperatures on substrates with a larger groove depth, it is also important to understand the effect of these temperature and geometry changes on the terminal speed and the torque.

4.3. Effect of operating temperature on rotation outputs

The variation of the terminal angular speed and torque with temperature for substrates with D=100 μm and 500 μm is shown in Fig. 6. Above the Leidenfrost temperature, the rotation dynamics do not demonstrate any significant difference between the superhydrophobic coated and uncoated substrates. Therefore, consistent with prior literature, the superhydrophobic coating smoothens the transition to the Leidenfrost regime [38] and enables self-propulsion below the Leidenfrost temperature [30]. Above the Leidenfrost temperature, the torque and terminal angular speed on freshly coated substrates and substrates subjected to multiple heating cycles did not show any significant differences. This observation suggests that any deterioration in our superhydrophobic coating had a marginal effect on the rotation outputs.

The variation of the rotation outputs with temperature shows two regimes: (1) at lower temperatures the speed and torque increase with temperature and (2) at higher temperatures the speed and torque do not change significantly with temperature. Both groove depths demonstrate the same behaviour but the transition between the two regimes occurs at different temperatures; the substrates with smaller groove depths have a lower transition temperature. Also, above the Leidenfrost temperature, the substrate with a deeper groove shows a higher torque and terminal speed. To explain the variation of these rotation outputs with temperature and allow for a possible central vapor bubble, we extend the simple analytical model (Eq. (2)) to include the fluid mechanics of the surface-tension coupled composite solid-liquid Leidenfrost rotor.

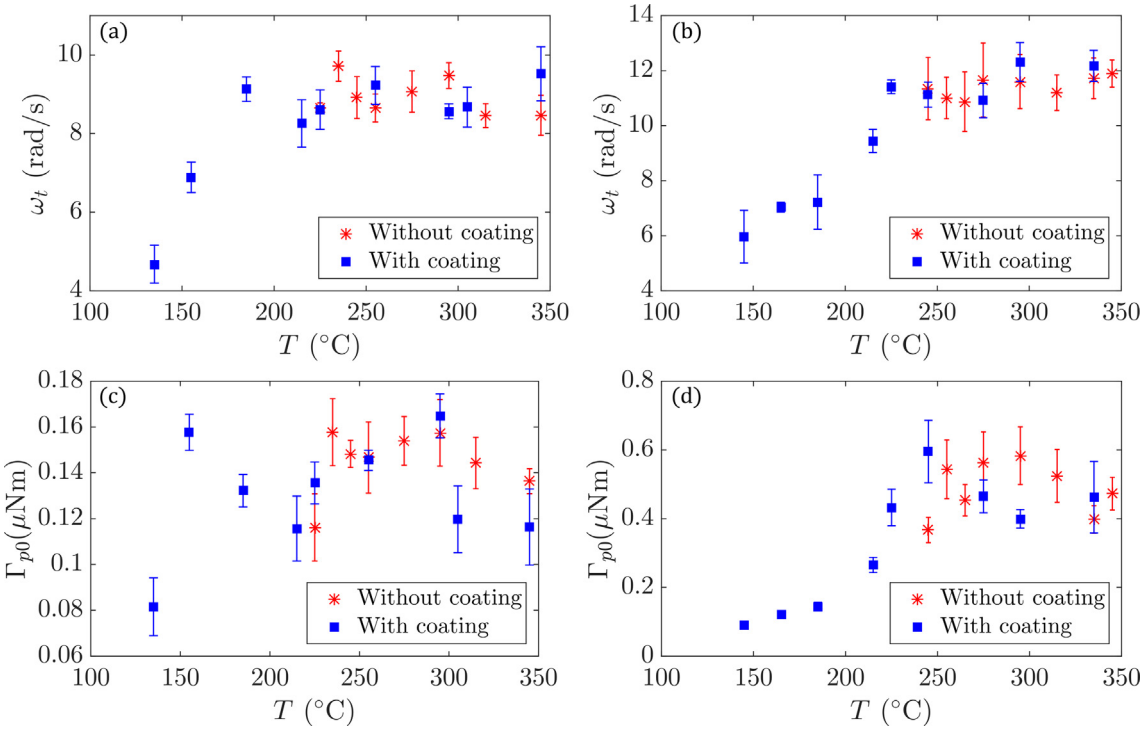

Fig. 6. Variation of terminal speed and torque for coated and uncoated substrates: (a) ω_t for D=100 μm, (b) ω_t for D=500 μm, (c) Γ_{p0} for D= 100 μm, (d) Γ_{p0} for D= 500 μm. The glass plate is not plasma cleaned in this dataset. The plate is cleaned by rinsing with IPA and DI water. The variation in temperature is ± 5 °C.

5. Analytical model and discussion

5.1. Equation of motion

A cross-sectional view of the different components of the Leidenfrost rotor is depicted in Fig. 7. We assume invariance along the angular coordinate. The resulting 2D axisymmetric model allows a vapor bubble in the liquid to be modelled by setting a non-zero value for the radius R_1. The angular speed of rotation of the liquid volume is assumed to be constant in the radial direction r, i.e. $\partial\omega/\partial r = 0$. The flow velocities in the r and z directions are assumed to be zero. We consider the liquid-vapor interface to be flat and have a uniform angular velocity ω_v. The solid-liquid interface moves at a uniform angular speed ω_p, with a no-slip condition.

Given the configuration of our Leidenfrost rotor, as depicted in Fig. 7, and the substrate geometry, we consider vapor rectification induced viscous stresses to be the dominant propulsion mechanism. The propulsion on our substrates is similar to that of drops on a herringbone pattern [19], where the macro texture of the substrate contributes to the anisotropic evacuation of vapor. In this case, for typical values of vapor layer thickness h_v= 100 μm, evaporation velocity v_0= 0.1 m/s, and substrate size R= 15mm, the vapor flow velocity exiting from the substrate is of the order of 10m/s. Considering a typical liquid volume thickness of H= 1mm, a balance of shear stress at the liquid-vapor interface results in typical speeds in the liquid volume of the order of 0.1 m/s. This is comparable to the experimentally observed rotational speed of the plate, which justifies the use of the viscous propulsion mechanism for the analytical model. In our model the viscous shear stress on the liquid-vapor interface is considered from vapor flow in the grooves only. Viscous stress originating from the vapor flow over the non-grooved part of the substrate is not considered.

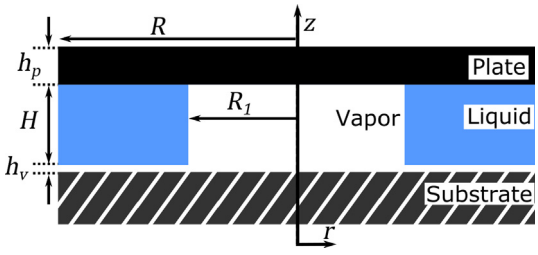

Fig. 7. Depiction of the different components of a Leidenfrost rotor (cross-section view). The vapor layer thickness over the non-grooved part of the substrate is indicated by h_v. The liquid volume has a thickness H and h_p is the thickness of the solid plate. The vapor bubble is considered to be cylindrical with radius R_1.

The propulsion torque generated in the vapor layer (Γ_v) is accompanied by viscous dissipation in the vapor layer (proportional to ω_v). A balance of shear stress at the liquid-vapor interface transfers this propulsion torque to the liquid volume. The deformation of the liquid-vapor interface over the substrate grooves (depicted in Fig. 8(a)) reduces the torque transfer by adding an inertial resistance (proportional to ω_p^2). The torque transmission from the liquid-vapor interface to the liquid-solid interface is further dissipated by viscous friction in the liquid volume (proportional to $\omega_v - \omega_p$). Assuming the inertial acceleration of the liquid volume to be proportional to $\dot{\omega}_p$, a torque balance on the liquid volume can be written as:

$$I_l\dot{\omega}_p + c_i\omega_p^2 = \Gamma_v - c_v\omega_v - c_l(\omega_v - \omega_p). \tag{3}$$

Here, c_v is the viscous damping coefficient in the vapor layer, c_l is the viscous damping coefficient in the liquid volume, c_i is the inertial damping coefficient and I_l is the moment of inertia of the liquid volume; $I_l = \pi(R^4 - R_1^4)\rho_l H$, where ρ_l is the density of the liquid. The shear stress generated at the liquid-vapor interface is transferred through viscous stresses in the liquid up to the solid plate. The equation of motion of the solid plate can be written as:

$$I_p\dot{\omega}_p = c_l(\omega_v - \omega_p), \tag{4}$$

where, I_p is the moment of inertia of the solid plate; $I_p = \pi R^4\rho_p h_p$, where ρ_p is the density of the plate and h_p is the thickness of the plate. Considering that the inertial resistance is higher than the viscous resistance by almost an order of magnitude [11,19], Eqs. (3) and (4) are reduced

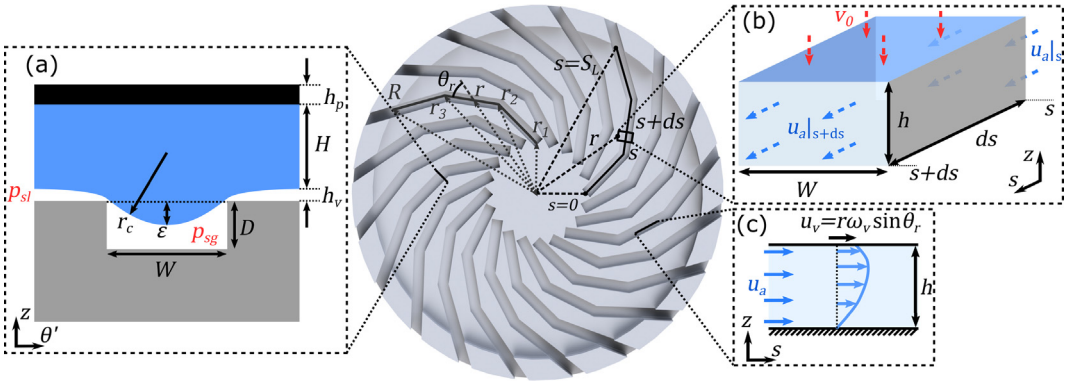

Fig. 8. (a) Depiction of the deformed liquid-vapor interface over a cross-section of the groove. p_{sl} is the vapor pressure in the non-grooved part of the substrate and p_{sg} is the vapor pressure in the groove. ε is the deformation of the liquid-vapor interface in the groove, assuming a radius of curvature r_c. (b) Depiction of the vapor flux in a section ds at an arc length s of the groove. v_0 is the evaporative flux from the liquid volume and u_a is the average vapor flow velocity along the groove. (c) Poiseuille-Couette flow in the sz cross-section of the groove. The Poiseuille flow is driven by the pressure difference from the vapor flow along the groove, indicated by the velocity profile u and average flow velocity u_a. The Couette flow is due to the rotation of the liquid-vapor interface indicated by the velocity u_v, which is the component of the liquid rotation velocity along the groove.

to:

$$(I_l + I_p)\dot{\omega}_p + c_i\omega_p^2 = \Gamma_v. \tag{5}$$

The solution to Eq. (5) can be written as:

$$\omega_p = \omega_t \tanh(t/\tau), \tag{6}$$

$$\omega_t = \sqrt{\frac{\Gamma_v}{c_i}}, \tag{7}$$

$$\tau = \frac{I_l + I_p}{\sqrt{\Gamma_v c_i}}. \tag{8}$$

The torque on the plate at $t = 0$ is obtained from $\Gamma_{p0} = I_p\omega_t/\tau$, as:

$$\Gamma_{p0} = \frac{I_p\Gamma_v}{I_l + I_p}. \tag{9}$$

The analytical formulation for the rotation of the plate obtained in Eq. (6) has the simple formulation derived in Eq. (2) as a limiting case. We now develop a model for the vapor and liquid flow to obtain analytical expressions for the terminal angular speed (ω_t) and torque (Γ_{p0}).

5.2. Hydrodynamic model

We first estimate the propulsion torque from the vapor layer (Γ_v) by analyzing the vapor flow in the substrate grooves. Let us assume that the vapor flow along the groove arc follows a Poiseuille-Couette flow in an infinitely wide parallel plate system, as depicted in Fig. 8(c). The Poiseuille flow is driven by the pressure difference due to the evaporative flux from the liquid (v_0), as depicted in Fig. 8(b). The Couette flow is due to the rotation of the liquid-vapor interface with velocity u_v along the groove arc.

The velocity flow profile u can be written as [49]:

$$u = \frac{u_v z}{h} - \frac{1}{2\mu_v}\frac{dp_{sg}}{ds}z(h - z), \tag{10}$$

where, p_{sg} is the pressure in the groove as depicted in Fig. 8(a), h is the height of the liquid-vapor interface above the groove base, $u_v = r\omega_v\sin\theta_r$ is the velocity of the liquid-vapor interface along the groove, as shown as Fig. 8(c), μ_v is the dynamic viscosity of the vapor and θ_r is the angle between the radial direction and the groove arc at the radial coordinate r. As the radial flows in the liquid volume are assumed to be zero, u_v comprises of only the angular velocity of the liquid-vapor interface along the groove. The average vapor flow velocity along the groove arc is given as, $u_a = \int_0^h u dz/h$. Therefore, by integrating Eq. (10) along z, we obtain the pressure gradient in the groove:

$$\frac{dp_{sg}}{ds} = \left(\frac{u_v}{2} - u_a\right)\frac{12\mu_v}{h^2}. \tag{11}$$

The velocity along the groove arc, u_a, can be estimated from a mass flux balance as shown in Fig. 8(b):

$$(hu_a)_{s+ds} - (hu_a)_s = v_0 ds, \tag{12}$$

which, on integration, gives:

$$u_a = \frac{v_0 s}{h}. \tag{13}$$

Here, s is the arc length of a groove at a radial coordinate r. Combining Eqs. (11), (12) and (13), the shear stress on the liquid-vapor interface is given by:

$$\mu_v\left(\frac{du}{dz}\right)_{z=h} = \frac{2\mu_v}{h}\left(\frac{3v_0 s}{h} - 2r\omega_v\sin\theta_r\right). \tag{14}$$

The evaporation velocity v_0 is obtained from an energy balance, assuming that the latent heat of evaporation is supplied by the substrate through conduction in the vapor layer, i.e. $k\Delta T/h = \rho_v L v_0$ [13]. Here, ρ_v is the density of the vapor layer, k is the thermal conductivity of the vapor layer, L is the latent heat of vaporization of the liquid, ΔT is the temperature difference between the substrate and the boiling point of the liquid. In this formulation we assume that the substrate temperature is uniform and that the distance between the liquid-vapor interface and the substrate is constant (equal to h).

From Eq. (13), the net torque due to the viscous stresses on the liquid-vapor interface can be written as:

$$\Gamma_f = N\int_{s_1}^{s_2}\mu_v r\left(\frac{du}{dz}\right)_{z=h}\sin\theta_r W ds. \tag{15}$$

Here, N is the number of grooves in the substrate. Including the presence of a vapor bubble with radius R_1, s_1 and s_2 represent the arc length corresponding to $r = R_1$ and $r = R$, respectively. The first term on the right in Eq. (14) gives the propulsion torque due to the liquid evaporation and the second term represents the viscous losses in the vapor layer. Therefore, Eq. (15) can be written as a sum of the propulsion torque (Γ_v) and viscous damping ($c_v\omega_v$):

$$\Gamma_f = \Gamma_v - c_v\omega_v. \tag{16}$$

Based on these considerations, we obtain an expression of the propulsion torque:

$$\Gamma_v = \frac{2\mu_v NWk\Delta T f(s, R_1, R)}{\rho_v L h^3}, \tag{17}$$

where, $f(s, R_1, R)$ is a function that depends on substrate geometry; complete expressions for Γ_v and c_v are given in the supplementary information.

To estimate the terminal angular speed from Eq. (7), we now look at the liquid volume to estimate the inertial damping coefficient c_i. As the liquid height is smaller in the non-grooved part of the substrate (Fig. 8(a)), the angular velocity will be slightly higher than that in the grooved part of the substrate. Therefore, the liquid must gain angular momentum to climb over the deformation in the grooves. The rate of change of this angular momentum gives an estimate of the inertial damping resistance. Denoting the average angular speed of the liquid over the grooves as ω_2 and over the non-grooved part as ω_1, a mass balance in an annulus of thickness dr at a radial distance r gives $r\omega_1 Hdr = r\omega_2(H+\varepsilon)dr$. Here, ε is the deformation of the liquid-vapor interface in the groove as depicted in Fig. 8(a). The rate of change of angular momentum (L_g) can be written as $L_g = \rho_l(r\omega_2)^2 Hdr - \rho_l(r\omega_1)^2(H+\varepsilon)dr$, where ρ_l is the density of the liquid. Considering $\varepsilon/H << 1$ and $\omega_2 \approx \omega_v$, integrating L_g over the entire liquid volume we get:

$$c_i\omega_v^2 = \left[\frac{\rho_l(R^4 - R_1^4)\varepsilon}{4} N sin\alpha\right]\omega_v^2. \tag{18}$$

Given the scale of R_1 from experiments, its effect on the total torque is not significant. Subsequently, for the considered geometry $f(s, R_1, R)$ in Eq. (17) can be written as $f(s, R_1, R) = c_t R^3$, where c_t is a numerical factor depending on the substrate geometry. Similarly, the inertial damping coefficient c_i can also be written as $c_i = \rho_l R^4 \varepsilon N \sin\alpha/4$. Using Eqs. (17) and (18), the expressions for the torque and terminal speed (from Eqs. (7) and (9)) are obtained as:

$$\Gamma_{p0} = \frac{2c_t\mu_v NWk\Delta T R^3 \rho_p h_p}{\rho_v L h^3(\rho_l H + \rho_p h_p)}, \tag{19}$$

$$\omega_t = \sqrt{\frac{8c_t\mu_v Wk\Delta T}{\rho_v\rho_l L h^3 R\varepsilon \sin\alpha}}. \tag{20}$$

The substrate temperature affects the vapor layer thickness h and the liquid deformation ε. Therefore, in Eqs. (19) and (20), to estimate the effect of the substrate temperature on the variation of ω_t and Γ_v, it is important to assess the effect of substrate temperature on h and ε. This assessment primarily includes the effect of deformation of the liquid-vapor interface in the groove on the rotation outputs.

5.3. Effect of liquid deformation over grooves

As opposed to solid blocks, liquid volumes deform over the grooves as depicted in Fig. 8(a), which gives the vapor layer thickness as $h = D - \varepsilon$. The deformation of the liquid-vapor interface (ε) can be expressed as a balance between the Laplace pressure, hydrostatic pressure and the vapor pressure in the groove (p_{sg}):

$$p_{sg} + \frac{\gamma}{r_c} = \rho_l(H+\varepsilon)g + \rho_p h_p g, \tag{21}$$

where, γ is the surface tension of the liquid-vapor interface, r_c is obtained from geometry considering a circular cross-section: $r_c^2 = (r_c - \varepsilon)^2 + W^2/4$. In the limit of $\varepsilon \ll W$, Eq. (21) can be written as:

$$\left(\frac{8\gamma}{W^2} - \rho_l g\right)\varepsilon = (\rho_l H + \rho_p h_p)g - p_{sg}, \tag{22}$$

where p_{sg} is a function of the arc length (s) and is derived by integrating Eq. (11) as:

$$p_{sg}(s) = p_{atm} + \frac{6\mu_v k\Delta T(S_l^2 - s^2)}{\rho_v L h^4}. \tag{23}$$

In the above equation, p_{sg} depends on the temperature difference and the groove depth. Although p_{sg} also depends on the vapor bubble size, we do not address this effect as the vapor bubble size is not an independently controllable parameter. Therefore, Eq. (23) considers the case where the liquid is spread fully over the substrate. At low substrate temperatures or large groove depths, p_{sg} is smaller than the hydrostatic pressure. In this state the liquid is in contact with the substrate, however, it is not pinned due to the low hysteresis provided by the superhydrophobic coating. As a result, ε and the vapor layer thickness remain independent of temperature. The torque and terminal speed power law scaling with respect to the temperature difference and groove depth can be written as:

$$\Gamma_{p0} \propto \frac{\Delta T}{(D-\varepsilon)^3}, \tag{24}$$

$$\omega_t \propto \frac{\Delta T^{1/2}}{\varepsilon^{1/2}(D-\varepsilon)^{3/2}}. \tag{25}$$

The angular speed scaling in this temperature regime agrees with the observations of Dupeux et al. for terminal velocity of droplets on superhydrophobic ratchets [30].

Our experiment data demonstrates good agreement with the linear and square root scaling of ΔT derived in Eqs. (24) and (25), as shown in the lower ΔT regime of Fig. 9(a) and (b). As the temperature increases, p_{sg} increases and it starts competing with the hydrostatic pressure, which decreases the deformation of the liquid-vapor interface in the grooves. At high temperatures, the liquid is completely pushed out of the grooves by the increasing vapor pressure and loses contact with the substrate, attaining a complete Leidenfrost state. In this case, the vapor layer thickness can be expressed as a balance of the hydrostatic pressure and the average vapor pressure in the grooves, which gives:

$$h \approx \left(\frac{3\mu_v k\Delta T S_l^2}{\rho_e h_e L \rho_l g}\right)^{1/4}, \tag{26}$$

where, $\rho_e h_e = \rho_l H + \rho_p h_p$. The vapor layer thickness obtained in Eq. (26) is similar to that for a drop on a smooth substrate [13]. Given Eq. (26), the torque and angular speed scaling in this regime can be obtained as:

$$\Gamma_{p0} \propto \Delta T^{1/4}, \tag{27}$$

$$\omega_t \propto \Delta T^{1/8}. \tag{28}$$

The above scaling shows that in this higher ΔT regime, the torque and angular speed are less sensitive to substrate temperature variations than in the low temperature regime, which agrees with previous experimental observations [8]. This weak power law scaling arises because of two competing effects: an increase in temperature increases the vapor flux, which increases the torque but also leads to a thicker vapor film that acts to decrease the torque. The angular speed scaling in Eq. (28) is similar to that obtained for drops in the Leidenfrost state over such rectangular cross-section grooved substrates [19]. The argument also broadly captures the transition to a less temperature sensitive regime apparent in the experimental observations (Fig. 9), although the model does not capture the precise exponents in the scaling at these higher values of ΔT.

The experiments also demonstrate that the transition between the two scaling regimes is observed at a lower temperature for the substrate with a smaller groove depth (Fig. 9). This behaviour can be explained by observing the effect of the groove depth on the vapor pressure from Eq. (23). For the same vapor pressure, a smaller groove depth will require a lower substrate temperature. Therefore, the temperature at which the vapor pressure in the groove becomes dominant will be lower for a substrate with a smaller groove depth. Our model qualitatively explains the effect of the groove depth on this transition temperature. To obtain an accurate quantitative estimate, additional information on the interaction of the deformable liquid-vapor interface with the groove

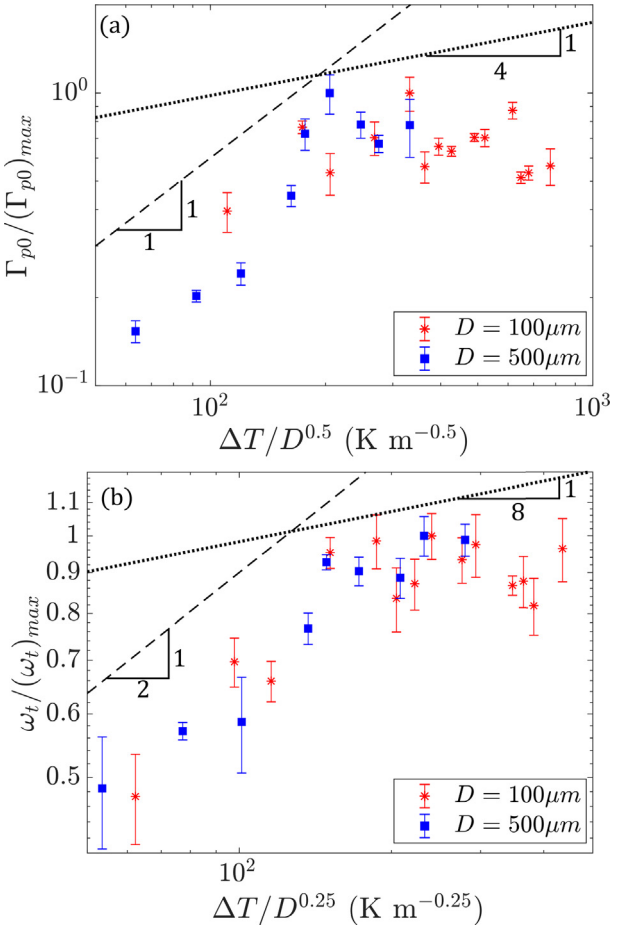

Fig. 9. Scaling for (a) normalized torque and (b) normalized terminal speed. The dashed lines represent the scaling for the low temperature regime (Eqs. (24) and (25)) and the dotted lines represent the scaling for the higher temperature regime (Eqs. (27) and (28)). The data has been normalized by the maximum values for the respective groove depths. For D=100 μm: $(\omega_t)_{max}$ = 9.6 rad/s and $(\Gamma_{p0})_{max}$ = 0.16 μNm. For D=500 μm: $(\omega_t)_{max}$ = 12.4 rad/s and $(\Gamma_{p0})_{max}$ = 0.6 μNm. The temperature difference ΔT on the x-axis is scaled with $D^{0.5}$ for the torque plot and $D^{0.25}$ for the terminal speed plot. These exponents were obtained by fitting the individual data sets. The variation in temperature is ± 5 °C.

geometry is needed. For instance, in a rectangular cross-section groove, the finite width of the groove adds additional heat sources close to the liquid-vapor interface. The interaction of these finite spaced heated walls with the deformed liquid-vapor interface alters the mass flux and introduces an additional temperature dependent length scale, which amplifies the effect of temperature on the deformation of the liquid-vapor interface in the groove.

The weak temperature dependence of both torque and angular speed above the Leidenfrost temperature (shown in Fig. 9) indicates a limit on the maximum power output from the rotation ($P_{rot} = \Gamma_{p0}\omega_t$). In this regime, although an increase in temperature increases the evaporative flux, it also increases the vapor layer thickness, which reduces the vapor pressure build up underneath the liquid. These two competing effects lead to a temperature invariance in the rotation outputs and limiting the power output above the Leidenfrost temperature. However, the variation of torque (and angular speed) below the Leidenfrost temperature demonstrates that if a constant vapor layer thickness can be maintained, a monotonic power output increase can be obtained with an increase in temperature. In the present work this is exemplified by using two substrates with different groove depths. In the substrate with the larger groove depth (D = 500 μm), the vapor pressure capable of sustaining levitation is obtained at a higher temperature than the substrate with D = 100 μm. Therefore, on the substrate with a larger groove depth the vapor layer thickness dependence on temperature is delayed, which increases the obtained torque and terminal speed for a larger temperature range than that obtained on the D = 100 μm substrate. Future designs can implement strategies to maintain a constant vapor layer thickness even above the Leidenfrost temperature as a measure to increase the power output.

The maximum theoretical thermodynamic efficiency of our conceptual Leidenfrost engine is equal to the Carnot efficiency, as discussed in Section 2. However, in practice, this efficiency does not consider the energy spent to sustain the levitation of the rotor, in the present earth-like atmospheric conditions, which accounts for the majority of the energy supplied for phase change [22]. In environments where volume effects are considerably small, such as in microgravity conditions of space or the high surface area to volume ratio environments at micro-scales, the energy spent in levitation can be significantly reduced, which can increase the available for rotation. Other factors that can enhance the efficiency are low pressures and working fluids with low latent heat of vaporization. Our proof-of-concept study employs water as a working fluid, which has a very high latent heat of vaporization. Using alternate working substances with lower latent heat of vaporization can reduce the heat input significantly (e.g. organics such as acetone and *iso*-propyl alcohol in inert environments). Similarly, operation in reduced atmospheric pressures can also lower the heat input for vaporization. These aspects present applications for space and planetary exploration, where locally occurring resources, such as alternate liquid working substances and naturally occurring low pressures and high temperature differences, can be used for in-situ power generation. In this regard, our results will inform the design and operation of such heat engines in these alternate environmental conditions.

6. Conclusion

In this work we have demonstrated the sustained rotation of a Leidenfrost rotor, where a solid component is coupled to a liquid volume in the Leidenfrost state over a turbine-inspired substrate. The sustained rotation was achieved by continuously feeding liquid, which supported a glass plate, over a heated substrate. As the substrate sizes used are significantly larger than the capillary length of the liquid, there is an increased tendency of a vapor bubble to form underneath the glass plate. The size of these vapor bubbles affects the stability of the rotation of the plate and the obtained torque. The use of a glass plate allows us to monitor the liquid distribution over the substrate and, therefore, assess methods to ensure a stable rotation. We find that by making the glass plate hydrophilic or superhydrophilic and using substrates with deeper grooves, the formation of the vapor bubble at the centre of the substrate is reduced. This leads to a better coupling between the solid and liquid components and a stable rotation of the Leidenfrost rotor. Using superhydrophobic substrate coatings we extended the operational range of the rotor to temperatures lower than the Leidenfrost point of the liquid on the substrate. As a result, we were able to assess the torque and terminal angular speed characteristics of the rotation over a temperature range of 130–350 °C. We observed two distinct regimes: (1) at lower temperatures the speed and the torque increase with the substrate temperature and, (2) at higher temperatures the torque and speed are largely independent of the temperature. The transition temperature of these regimes depends on the depth of the grooves, where the shallow grooved substrate encounters a lower transition temperature. We have quantified this behaviour using a hydrodynamic model that considers the deformation of the liquid-vapor interface over the grooves of the substrate. Our results demonstrate the continuous conversion of thermal energy to mechanical energy which is a critical step in enabling the construction of low-friction Leidenfrost-based mechanical and heat engines with a closed thermodynamic cycle. Such low-friction engines can resolve friction-induced wear and fatigue at

microscales for potential applications in thermal energy harvesting. At macroscales, these engines show prospects in exploiting extreme environmental conditions and locally available resources for power generation in deep-space and planetary exploration.

Acknowledgements

We would like to thank funding from EPSRC grants EP/P005896/1 and EP/P005705/1. We thank Prof. Anthony Walton for fruitful discussions. We also thank Mr. Sam Hutchinson, Mr. Simon Neville and Mr. Phillip Donelly for machining the substrates.

Appendix A. Supplementary material

Supplementary data to this article can be found online at https://doi.org/10.1016/j.apenergy.2019.02.034.

References

[1] Ammar Y, Joyce S, Norman R, Wang Y, Roskilly AP. Low grade thermal energy sources and uses from the process industry in the UK. Appl Energy 2012;89:3–20. https://doi.org/10.1016/j.apenergy.2011.06.003.
[2] Roy JP, Mishra MK, Misra A. Performance analysis of an Organic Rankine Cycle with superheating under different heat source temperature conditions. Appl Energy 2011;88:2995–3004. https://doi.org/10.1016/j.apenergy.2011.02.042.
[3] Mueller RP, Sibille L, Mantovani J, Sanders GB, Jones CA. Opportunities and strategies for testing and infusion of ISRU in the evolvable mars campaign. In: AIAA SPACE 2015 Conference and Exposition, American Institute of Aeronautics and Astronautics; 2015. http://doi.org/10.2514/6.2015-4459.
[4] Palaszewski B. Solar system exploration augmented by in-situ resource utilization: Human planetary base issues for Mercury and Saturn. In: 10th Symposium on Space Resource Utilization, 2017; 2017. https://www.scopus.com/inward/record.uri?eid=2-s2.0-85017360532&partnerID=40&md5=ff9741b18ea416b3aeb0cf3e459b9f24.
[5] Ku ISY, Reddyhoff T, Holmes AS, Spikes HA. Wear of silicon surfaces in MEMS. Wear 2011;271:1050–8. https://doi.org/10.1016/j.wear.2011.04.005.
[6] McCarthy M, Waits CM, Ghodssi R. Dynamic friction and wear in a planar-contact encapsulated microball bearing using an integrated microturbine. J Microelectromech Syst 2009;18:263–73. https://doi.org/10.1109/JMEMS.2009.2013407.
[7] Leidenfrost JG. On the fixation of water in diverse fire. Int J Heat Mass Transf 1966;9:1153–66. https://doi.org/10.1016/0017-9310(66)90111-6.
[8] Linke H, Alemán BJ, Melling LD, Taormina MJ, Francis MJ, Dow-Hygelund CC, et al. Self-propelled leidenfrost droplets. Phys Rev Lett 2006;96:2–5. https://doi.org/10.1103/PhysRevLett. 96.154502.
[9] Janssens SD, Koizumi S, Fried E. Behavior of self-propelled acetone droplets in a Leidenfrost state on liquid substrates. Phys Fluids 2017;29. https://doi.org/10.1063/1.4977442.
[10] Ok JT, Choi J, Brown E, Park S. Effect of different fluids on rectified motion of Leidenfrost droplets on micro/sub-micron ratchets. Microelectron Eng 2016;158:130–4. https://doi.org/10.1016/j.mee.2016.04.018.
[11] Lagubeau G, Le Merrer M, Clanet C, Quéré D. Leidenfrost on a ratchet. Nat Phys 2011;7:395–8. https://doi.org/10.1038/nphys1925.
[12] Diniega S, Hansen CJ, McElwaine JN, Hugenholtz CH, Dundas CM, McEwen AS, et al. A new dry hypothesis for the formation of martian linear gullies. Icarus 2013;225:526–37. https://doi.org/10.1016/j.icarus.2013.04.006.
[13] Biance AL, Clanet C, Quéré D. Leidenfrost drops. Phys Fluids 2003;15:1632–7. https://doi.org/10.1063/1.1572161.
[14] Bouillant A, Mouterde T, Bourrianne P, Lagarde A, Clanet C, Quéré D. Leidenfrost wheels. Nat Phys 2018. https://doi.org/10.1038/s41567-018-0275-9.
[15] Dupeux G, Le Merrer M, Lagubeau G, Clanet C, Hardt S, Quéré D. Viscous mechanism for Leidenfrost propulsion on a ratchet. EPL (Europhys Lett) 2011;96:58001. https://doi.org/10.1209/0295-5075/96/58001.
[16] Sibille L, Mantovani JG, Dominguez JA. In-space propulsion engine architecture based on sublimation of planetary resources: from exploration robots to NEO mitigation. Earth Space 2012:479–88. https://doi.org/10.1061/9780784412190.051.
[17] Mrinal M, Wang X, Luo C. Self-rotation-induced propulsion of a Leidenfrost drop on a ratchet. Langmuir 2017;33:6307–13. https://doi.org/10.1021/acs.langmuir.7b01420.
[18] Würger A. Leidenfrost gas ratchets driven by thermal creep. Phys Rev Lett 2011;107:1–4. https://doi.org/10.1103/PhysRevLett. 107.164502.
[19] Soto D, Lagubeau G, Clanet C, Quere D. Surfing on a herringbone. Phys Rev Fluids 2016;013902:2–3. https://doi.org/10.1103/PhysRevFluids. 1.013902.
[20] Baier T, Dupeux G, Herbert S, Hardt S, Quéré D. Propulsion mechanisms for Leidenfrost solids on ratchets. Phys Rev E - Stat, Nonlin, Soft Matter Phys. 2013;87:3–6. https://doi.org/10.1103/PhysRevE.87.021001.
[21] Cousins TR, Goldstein RE, Jaworski JW, Pesci AI. A ratchet trap for Leidenfrost drops. J Fluid Mech 2012;696:215–27. https://doi.org/10.1017/jfm.2012.27.
[22] Wells GG, Ledesma-Aguilar R, McHale G, Sefiane K. A sublimation heat engine. Nat Commun 2015;6:6390. https://doi.org/10.1038/ncomms7390.
[23] hai Jia Z, yao Chen M, tao Zhu H. Reversible self-propelled Leidenfrost droplets on ratchet surfaces. Appl Phys Lett 2017;110:091603. https://doi.org/10.1063/1.4976748.
[24] Agapov RL, Boreyko JB, Briggs DP, Srijanto BR, Retterer ST, Collier CP, et al. Length scale of Leidenfrost ratchet switches droplet directionality. Nanoscale 2014;6:9293–9. https://doi.org/10.1039/c4nr02362e.
[25] Agapov RL, Boreyko JB, Briggs DP, Srijanto BR, Retterer ST, Collier CP, et al. Asymmetric wettability of nanostructures directs Leidenfrost droplets. ACS Nano 2014;8:860–7. https://doi.org/10.1021/nn405585m.
[26] Dupeux G, Baier T, Bacot V, Hardt S, Clanet C, Quéré D. Self-propelling uneven Leidenfrost solids. Phys Fluids 2013;25:1–7. https://doi.org/10.1063/1.4807007.
[27] Soto D, De Maleprade H, Clanet C, Quéré D. Air-levitated platelets: from take off to motion. J Fluid Mech 2017;814:535–46. https://doi.org/10.1017/jfm.2017.27.
[28] Hashmi A, Xu Y, Coder B, Osborne Pa, Spafford J, Michael GE, Yu G, Xu J. Leidenfrost levitation: beyond droplets. Sci Rep 2012;2:797. https://doi.org/10.1038/srep00797.
[29] Shi M, Ji X, Feng S, Yang Q, Lu TJ, Xu F. Self-propelled hovercraft based on cold Leidenfrost phenomenon. Sci Rep 2016;6:1–7. https://doi.org/10.1038/srep28574.
[30] Dupeux G, Bourrianne P, Magdelaine Q, Clanet C, Quéré D. Propulsion on a superhydrophobic ratchet. Sci Rep 2014;4:5280. https://doi.org/10.1038/srep05280.
[31] Dodd LE, Wood D, Geraldi NR, Wells GG, McHale G, Xu BB, et al. Low friction droplet transportation on a substrate with a selective Leidenfrost effect. ACS Appl Mater Interfaces 2016;8:22658–63. https://doi.org/10.1021/acsami.6b06738.
[32] Bell LE. Cooling, heating, generating power, and recovering waste heat with thermoelectric systems. Science 2008;321:1457–61. https://doi.org/10.1126/science.1158899.
[33] Kishore R, Priya S. A review on low-grade thermal energy harvesting: materials, methods and devices. Materials. 2018;11:1433. https://doi.org/10.3390/ma11081433.
[34] Orejon D, Sefiane K, Takata Y. Effect of ambient pressure on Leidenfrost temperature. Phys Rev E - Stat Nonlin, Soft Matter Phys 2014;90:1–6. https://doi.org/10.1103/PhysRevE.90.053012.
[35] Celestini F, Frisch T, Pomeau Y. Room temperature water Leidenfrost droplets. Soft Matter 2013;9:9535–8. https://doi.org/10.1039/c3sm51608c.
[36] Sharon A, Bankoff SG. Destabilization of Leidenfrost boiling by a sudden rise of ambient pressure. Chem Eng Sci 1982;37:1173–9. https://doi.org/10.1016/0009-2509(82)85061-6.
[37] Emmerson GS. The effect of pressure and surface material on the Leidenfrost point of discrete drops of water. Int J Heat Mass Transf 1975;18:381–6. https://doi.org/10.1016/0017-9310(75)90027-7.
[38] Vakarelski IU, Patankar NA, Marston JO, Chan DYC, Thoroddsen ST. Stabilization of Leidenfrost vapour layer by textured superhydrophobic surfaces. Nature 2012;489:274–7. https://doi.org/10.1038/nature11418.
[39] Geraldi NR, McHale G, Xu BB, Wells GG, Dodd LE, Wood D, et al. Leidenfrost transition temperature for stainless steel meshes. Mater Lett 2016;176:205–8. https://doi.org/10.1016/j.matlet.2016.04.124.
[40] Kwon HM, Bird JC, Varanasi KK. Increasing Leidenfrost point using micro-nano hierarchical surface structures. Appl Phys Lett 2013;103:201601. https://doi.org/10.1063/1.4828673.
[41] Hays R, Maynes D, Crockett J. Thermal transport to droplets on heated superhydrophobic substrates. Int J Heat Mass Transf 2016;98:70–80. https://doi.org/10.1016/j.ijheatmasstransfer.2016.03.011.
[42] Clavijo CE, Crockett J, Maynes D. Hydrodynamics of droplet impingement on hot surfaces of varying wettability. Int J Heat Mass Transf 2017;108:1714–26. https://doi.org/10.1016/j.ijheatmasstransfer.2016.12.076.
[43] Perrard S, Couder Y, Fort E, Limat L. Leidenfrost levitated liquid tori. EPL 2012;100:54006. https://doi.org/10.1209/0295-5075/100/54006.
[44] Darbois Texier B, Piroird K, Quéré D, Clanet C. Inertial collapse of liquid rings. J Fluid Mech 2013;717:R3. https://doi.org/10.1017/jfm.2013.15.
[45] Celestini F, Frisch T, Cohen A, Raufaste C, Duchemin L, Pomeau Y. Two dimensional Leidenfrost droplets in a Hele-Shaw cell. Phys Fluids 2014;26:032103. https://doi.org/10.1063/1.4867163.
[46] Caswell TA. Dynamics of the vapor layer below a Leidenfrost drop. Phys Rev E - Stat, Nonlin, Soft Matter Phys 2014;90:1–10. https://doi.org/10.1103/PhysRevE.90.013014.
[47] Burton JC, Sharpe AL, Van Der Veen RCA, Franco A, Nagel SR. Geometry of the vapor layer under a Leidenfrost drop. Phys Rev Lett 2012;109:1–4. https://doi.org/10.1103/PhysRevLett. 109.074301.
[48] Paul G, Manna I, Kumar Das P. Formation, growth, and eruption cycle of vapor domes beneath a liquid puddle during Leidenfrost phenomena. Appl Phys Lett 2013;103:084101. https://doi.org/10.1063/1.4819095.
[49] Batchelor GK. An Introduction to Fluid Dynamics, Cambridge: Cambridge University Press; 2000. http://doi.org/10.1017/CBO9780511800955.